

UNCOVER: The rest ultraviolet to near infrared multiwavelength structures and dust distributions of sub-millimeter-detected galaxies in Abell 2744

SEDONA H. PRICE,¹ KATHERINE A. SUESS,^{2,*} CHRISTINA C. WILLIAMS,^{3,4} RACHEL BEZANSON,¹ GOURAV KHULLAR,¹
ERICA J. NELSON,⁵ BINGJIE WANG (王冰洁),^{6,7,8} JOHN R. WEAVER,⁹ SEIJI FUJIMOTO,^{10,*} VASILY KOKOREV,¹¹
JENNY E. GREENE,¹² GABRIEL BRAMMER,¹³ SAM E. CUTLER,⁹ PRATIKA DAYAL,¹¹ LUKAS J. FURTAJ,¹⁴ IVO LABBE,¹⁵
JOEL LEJA,^{6,7,8} TIM B. MILLER,¹⁶ THEMIYA NANAYAKKARA,¹⁷ RICHARD PAN,¹⁸ AND KATHERINE E. WHITAKER^{9,19}

¹*Department of Physics and Astronomy and PITT PACC, University of Pittsburgh, Pittsburgh, PA 15260, USA*

²*Kavli Institute for Particle Astrophysics and Cosmology and Department of Physics, Stanford University, Stanford, CA 94305, USA*

³*NSF's National Optical-Infrared Astronomy Research Laboratory, 950 N. Cherry Avenue, Tucson, AZ 85719, USA*

⁴*Steward Observatory, University of Arizona, 933 North Cherry Avenue, Tucson, AZ 85721, USA*

⁵*Department for Astrophysical and Planetary Science, University of Colorado, Boulder, CO 80309, USA*

⁶*Department of Astronomy & Astrophysics, The Pennsylvania State University, University Park, PA 16802, USA*

⁷*Institute for Computational & Data Sciences, The Pennsylvania State University, University Park, PA 16802, USA*

⁸*Institute for Gravitation and the Cosmos, The Pennsylvania State University, University Park, PA 16802, USA*

⁹*Department of Astronomy, University of Massachusetts, Amherst, MA 01003, USA*

¹⁰*Department of Astronomy, The University of Texas at Austin, Austin, TX 78712, USA*

¹¹*Kapteyn Astronomical Institute, University of Groningen, 9700 AV Groningen, The Netherlands*

¹²*Department of Astrophysical Sciences, Princeton University, 4 Ivy Lane, Princeton, NJ 08544*

¹³*Cosmic Dawn Center (DAWN), Niels Bohr Institute, University of Copenhagen, Jagtvej 128, København N, DK-2200, Denmark*

¹⁴*Physics Department, Ben-Gurion University of the Negev, P.O. Box 653, Be'er-Sheva 84105, Israel*

¹⁵*Centre for Astrophysics and Supercomputing, Swinburne University of Technology, Melbourne, VIC 3122, Australia*

¹⁶*Center for Interdisciplinary Exploration and Research in Astrophysics (CIERA) and Department of Physics & Astronomy, Northwestern University, IL 60201, USA*

¹⁷*Centre for Astrophysics and Supercomputing, Swinburne University of Technology, PO Box 218, Hawthorn, VIC 3122, Australia*

¹⁸*Department of Physics and Astronomy, Tufts University, 574 Boston Ave., Medford, MA 02155, USA*

¹⁹*Cosmic Dawn Center (DAWN), Denmark*

ABSTRACT

With the wavelength coverage, sensitivity, and high spatial resolution of JWST, it is now possible to peer through the dust attenuation to probe the rest-frame near infrared (NIR) and stellar structures of extremely dusty galaxies at cosmic noon ($z \sim 1 - 3$). In this paper we leverage the combined ALMA and JWST/HST coverage in Abell 2744 to study the multiwavelength ($0.5 - 4.4\mu\text{m}$) structures of 11 sub-millimeter (sub-mm) detected galaxies at $z \sim 0.9 - 3.5$ that are fainter than bright “classical” sub-mm galaxies (SMGs). While these objects reveal a diversity of structures and sizes, all exhibit decreasing sizes and increasing central concentration towards longer wavelengths. The smaller sizes of these objects at long wavelengths indicate that their stellar mass profiles are more compact than their optical light profiles, likely due to centrally-concentrated dust obscuration. Further, we find that galaxies with higher central concentration values tend to have more extreme size ratios (comparing the rest-frame NIR to rest-frame optical); this suggests that the galaxies with the most compact light distributions also have the most concentrated dust distributions. We also find the galaxies with the most extreme size ratios do not have elevated 1.2mm flux densities compared to the rest of our sample: we argue this means compact dust geometry, rather than e.g. high total dust quantity, drives the most extreme observed rest-frame NIR-to-optical size ratios. Upcoming higher resolution 1.2mm ALMA imaging will facilitate joint spatially-resolved analysis and will directly test the dust distributions within this representative sub-mm population.

Keywords: Galaxy formation (595); Galaxy evolution (594); Galaxy structure (622); Galaxy radii (617)

1. INTRODUCTION

The universe looks very different in the sub-millimeter (sub-mm) than at shorter wavelengths. Galaxies which are bright in the sub-mm are often faint or undetected at optical or near infrared (NIR) wavelengths, as their high dust content attenuates the shorter wavelength light and then re-emits this energy as thermal continuum in sub-mm to millimeter (mm) wavelengths (e.g., Casey et al. 2014). These sub-mm detected galaxies are typically distant ($z \gtrsim 1$), massive, dusty, and star-forming (e.g., Casey et al. 2014, Smith et al. 2017, Dudzevičiūtė et al. 2020; Hodge & da Cunha 2020). However, their detailed rest-frame NIR structures, which contain key information about their formation, remained uncertain with previously available observations.

The sensitivity of sub-mm and mm interferometers, particularly ALMA, has opened a window to directly study the impacts of dust well below the limits of ultraluminous infrared galaxies (ULIRGs) and classical bright sub-millimeter galaxies (SMGs), revealing dust continuum and obscured star formation even in “main sequence” star-forming galaxies. Probing the faint sub-mm population requires deep field or lensing cluster surveys, and there have been relatively limited ALMA studies in the $\sim 0.1 - 1$ mJy flux density regime to date (e.g., Fujimoto et al. 2016, Aravena et al. 2016, González-López et al. 2020, Gómez-Guijarro et al. 2022, Muñoz Arancibia et al. 2023). However, these surveys have shown that the dust content in the fainter population is still significant, with $\sim 85\%$ of star formation at cosmic noon ($z \sim 1 - 3$) obscured by dust (e.g., Dunlop et al. 2017). Thus, a full picture of galaxy assembly at cosmic noon requires an understanding of these lower sub-mm luminosity sources.

While the detailed substructures of bright dusty objects such as SMGs have been accessible with ALMA and NOEMA (revealing merging starbursts as well as disks; e.g., Hodge et al. 2016, 2019, Rujopakarn et al. 2016, Calistro Rivera et al. 2018, Lang et al. 2019, Puglisi et al. 2019, Tadaki et al. 2020), reaching the fainter population at high spatial resolution to map the dust continuum has remained a challenge, requiring very long exposures even with ALMA’s sensitivity. Little is known about this population’s intrinsic structures, including their distribution of dust and active star formation, leaving us without a complete picture of how this faint sub-mm population builds up or whether this population repre-

sents a particular evolutionary phase in galaxy formation.

An alternative, complementary avenue to characterize the dust distribution and obscured structures in faint sub-mm sources is using high-resolution rest-optical imaging to probe the stellar distribution directly. Prior to JWST, the high spatial resolution and sensitivity *Hubble Space Telescope* (HST) enabled detailed structural measurements, but its limited wavelength coverage (up to $\sim 1.6\mu\text{m}$) probed only as far as the rest frame optical at cosmic noon. And while *Spitzer* had longer wavelength coverage to probe the rest-frame near infrared (NIR) at these redshifts, it lacked the spatial resolution necessary to map stellar structures. Consequently, past structural measurements have typically been based on one HST filter at the rest-optical. However, dust complicates the interpretation of galaxies’ rest-optical structures. In particular, dust (as well as age and metallicity, which also contribute to radial color gradients) has been shown to result in dramatically different stellar size estimates depending on the dust concentration and distribution, as probed by relative differences between half-mass and half-light sizes (e.g., Wuyts et al. 2012, Liu et al. 2016, 2017, Suess et al. 2019, Miller et al. 2023, Zhang et al. 2023). Mock observations have also found dust geometry to be a major complication in structural interpretation of dusty galaxies (Popping et al. 2022, Zhang et al. 2023).

With the launch of JWST (Gardner et al. 2023), it is now possible to obtain high resolution imaging over an expanded wavelength range from $\lesssim 1\mu\text{m}$ out to $\sim 4.4\mu\text{m}$ (corresponding to the rest-frame $\sim 0.3 - 1.4\mu\text{m}$ at $z \sim 1 - 3$), providing information across the full stellar spectral energy distribution (SED). Critically, this coverage includes the rest-frame NIR probing the largely unattenuated stellar continuum. In addition to enabling robust measurements of sizes and stellar densities, comparing the rest-frame NIR with the rest-frame UV/optical (“color gradients”) allows us to constrain radial variations in mass-to-light ratios. These color gradients can be driven by non-uniform dust distributions or variations in relative stellar ages and/or metallicities; therefore, color gradients also indicate where active growth occurs in galaxies now relative to their past (e.g., Suess et al. 2021, 2022, 2023). Early results from JWST point to dust distribution as a major contributor to observed color profiles (e.g., Miller et al. 2022; also Suess et al. 2022) and without the simultaneous rest-NIR coverage, intrinsic size estimates may be biased towards larger values (e.g., Zhang et al. 2023, among others).

* NHFP Hubble Fellow

By combining JWST/NIRCam imaging with existing shorter wavelength HST imaging, we can now perform detailed multiwavelength structural studies of the distribution of stars, dust, and star formation in extremely dusty distant galaxies, revealing new insights about the nature and formation of this population. A number of studies have already leveraged early JWST observations to constrain the structures of distant dusty galaxies, including both sub-mm detected galaxies (including Cheng et al. 2022, 2023, Gillman et al. 2023, Kokorev et al. 2023, Rujopakarn et al. 2023, Smail et al. 2023, Wu et al. 2023, Boogaard et al. 2023) and other dusty galaxies (e.g., Gómez-Guijarro et al. 2023, Le Bail et al. 2023, Liu et al. 2023, Nelson et al. 2023, Magnelli et al. 2023). Building upon these works, we study the structures of a sample of galaxies within a cluster field, where the strong lensing boost allows us to examine the relation between total dust content and detailed multiwavelength structures for a variety of galaxies pushing to faint intrinsic fluxes and compact physical sizes.

Here we present a multiwavelength ($0.5 - 4.4\mu\text{m}$) structural analysis of 11 $z \sim 0.9 - 3.5$ sub-mm detected ($S_{1.2\text{mm,int}} \sim 0.2 - 1.5\text{mJy}$) galaxies in the Abell 2744 cluster field as measured with HST and JWST. This sample includes all galaxies detected in 1.2 mm ALMA continuum observations of the Abell 2744 primary cluster core from the ALMA Lensing Cluster Survey (ALCS; Fujimoto et al. 2023a) and ALMA-Hubble Frontier field (ALMA-HFF; Muñoz Arancibia et al. 2023) programs. We visually examine the rest-optical and NIR structures, then quantify the multiwavelength structures by fitting single component models and deriving residual-corrected flux profiles in every filter for the full sample. We also calculate the ratio of sizes between long ($> 4.4\mu\text{m}$) and short ($\sim 1.5 - 2.7\mu\text{m}$) wavelengths, which is sensitive to color gradient strengths probing radial changes in dust, age, or metallicity — and should be primarily driven by the dust in these extremely attenuated systems. Finally, we examine the structural measurements together with the intrinsic, lensing-corrected 1.2mm flux densities, to probe the impact of both dust quantity and geometry on these galaxies’ multiwavelength structures.

Throughout this work we adopt a flat ΛCDM cosmology with $H_0 = 70\text{ km s}^{-1}\text{ Mpc}^{-1}$, $\Omega_M = 0.3$, and $\Omega_\Lambda = 0.7$.

2. DATA

To study the rest-frame UV to near infrared (NIR) structures of sub-mm detected galaxies at cosmic noon ($z \sim 1 - 3$), we leverage the combination of low spa-

tial resolution ALMA continuum observations (beam FWHM $\sim 0.9'' \times 0.7''$; Fujimoto et al. 2023a) with deep, high spatial resolution JWST/HST coverage available for the Abell 2744 cluster field. We select galaxies from ALCS (Kokorev et al. 2022, Sun et al. 2022, Fujimoto et al. 2023a; including ALMA-HFF observations; González-López et al. 2017, Muñoz Arancibia et al. 2023), as presented in Fujimoto et al. (2023a). We include both sources in the ALCS 1.2mm continuum blind ($\text{SNR}_{\text{natural map}} \geq 5$; $N = 6$) and IRAC-prior ($4.0 \leq \text{SNR}_{\text{natural map}} < 5$ and $\text{SNR}_{\text{IRAC,CH2}} \geq 5$; $N = 5$) detection catalogs, for a total of 11 galaxies.

For this analysis, we use all public JWST/NIRCam (F115W, F150W, F200W, F277W, F356W, F410M, F444W) and HST/ACS (F435W, F606W, F814W) and WFC3 (F105W, F125W, F140W, F160W) imaging covering Abell 2744. Mosaics for all filters are produced with a common WCS grid using `grizli` (1.8.16.dev12; Brammer 2019, Kokorev et al. 2022) and `astrodrizzle` (Gonzaga et al. 2012), with JWST/NIRCam short wavelength (SW; F115W, F150W, F200W) filters drizzled onto a 20mas scale, while JWST/NIRCam long wavelength (LW; F277W, F356W, F410M, F444W) and HST filters are drizzled onto a 40 mas scale.¹ See Bezanson et al. (2022) for full details of the imaging reduction and mosaicing. Background subtraction and modeling and subtraction of bright cluster galaxies is then performed, as detailed in Weaver et al. (2023).

The ALCS sources are matched to JWST-detected sources from the UNCOVER photometric catalog (DR2; Weaver et al. 2023) with a search radius of $0.5''$. NIR counterparts for all ALCS sources are identified. However, in two cases (UNCOVER IDs 9018, 24143; denoted throughout with an asterisk), visual inspection reveals the galaxies are shredded into multiple sources in the UNCOVER catalog as a result of the detection deblending thresholds, which were optimized to detect faint, high-redshift sources. As the photometry and segmentation maps are used for simultaneous modeling or masking of neighboring objects in the structural modeling (see Sec. 3), for these two objects we instead perform an alternative detection (using SEP; Barbary 2018) with less aggressive deblending parameters (KERNEL=3.5 pixel FWHM Gaussian, MINAREA=3 pixels, THRESH=0.8 σ , DEBLEND_NTHRESH=8, DEBLEND_CONT=0.0001, CLEAN=Y, CLEAN_PARAM=1.0), and use the resulting segmentation maps and photometric parameters (derived using the same photometric pipeline as except for the parameter changes) for

¹ <https://s3.amazonaws.com/grizli-v2/JwstMosaics/v7/index.html>



Figure 1. RGB composite images (F115W+F150W/F200W+F277W/F356W+F410M+F444W; PSF-matched to F444W) of the sample, in decreasing order of F444W residual-corrected effective radii (R_E). The galaxy IDs from UNCOVER (Weaver et al. 2023) and ALCS (Fujimoto et al. 2023a) are noted in each panel, and the outlines show the colors used to denote each galaxy throughout the paper. Asterisks on the UNCOVER IDs (i.e., 9018, 24143) indicate that the alternative, less aggressively-deblended segmentation was used for structural modeling (see Sec. 2).

structural modeling of these two galaxies. We calculate the magnifications (μ) for each object from the updated lensing model by Furtak et al. (2023, v1.1), adopting the best-available redshifts. We also estimate stellar masses from the HST and JWST photometry, as well as the 1.2mm ALMA fluxes (from the most recent DUALZ catalog; Fujimoto et al. 2023b) using the same procedure as the UNCOVER DR2 stellar population synthesis (SPS) catalog (Wang et al. 2023), with the following modifications. First, we fix the redshifts to z_{spec} or z_{gris} when available. Second, we use the alternative, less deblended photometry measured for the aforementioned two objects. For the single object with only a z_{phot} (16840), we use the redshift and stellar mass directly from the DR2 SPS catalog (Wang et al. 2023). For clarity, we emphasize that all physical properties (i.e., stellar mass

and physical size) and the intrinsic 1.2mm flux densities are corrected for gravitational lensing using the magnification μ .

Color composite JWST images for our sample are shown in Fig. 1, and the sample IDs, positions, best-available redshifts, magnifications, and stellar masses are listed in Table 1. For structural modeling, we use empirical PSFs constructed for each band from unsaturated stars within the mosaic, renormalized so the energy enclosed within $4''$ aligns with typical calibration levels (see Weaver et al. 2023 for full details).

3. METHODS

To measure the multiwavelength structural parameters of our sample, we perform single Sérsic component fits in the image plane using GALFIT (Peng et al.

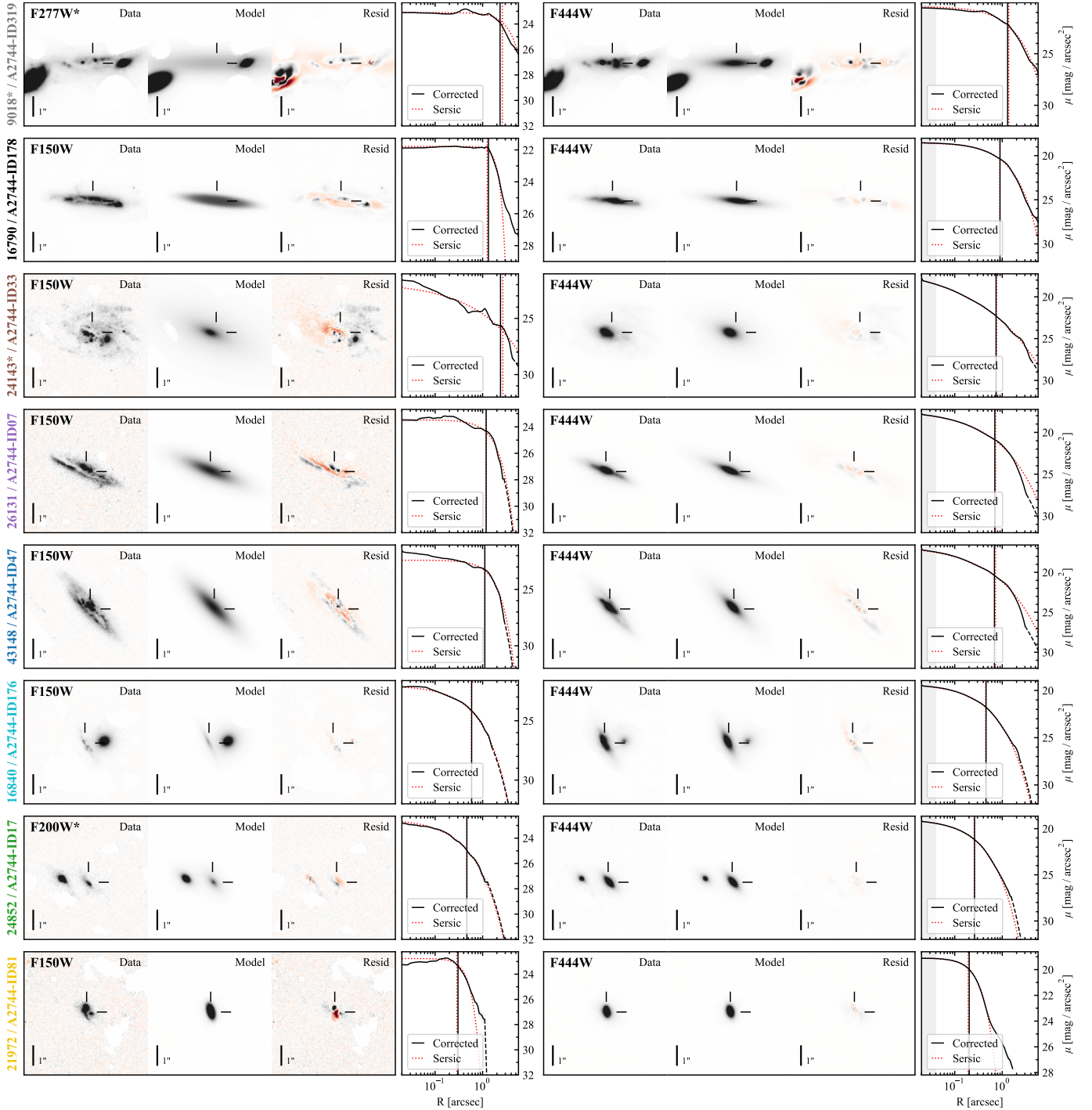


Figure 2. Example structural modeling for a short (*left*; F150W if fit and unflagged, otherwise F200W) and long wavelength band (*right*; F444W) for each galaxy. For each object and filter, we show postage stamps of the galaxy, the best-fit GALFIT model, and the residual (*leftmost 3 panels*, respectively), using the same linear color scale for all three images and cropped to 75% of the fit extent (i.e., $6'' \times 6''$) for clarity. The residual-corrected and best-fit Sérsic model surface brightness (SB) profiles are also shown (black and red dashed lines, respectively; *rightmost panel*), with the effective radii of each curve (R_E , $R_{E,S}$) denoted by the corresponding vertical line. For the residual-corrected SB profile, the uncertainty is shown with the shaded black region, and the dashed portion of the curve marks where the extrapolated Sérsic profile is adopted due to limited signal-to-noise. The vertical gray region indicates radii smaller than the pixel scale ($0.02''$, $0.04''$ for SW and LW bands, respectively).

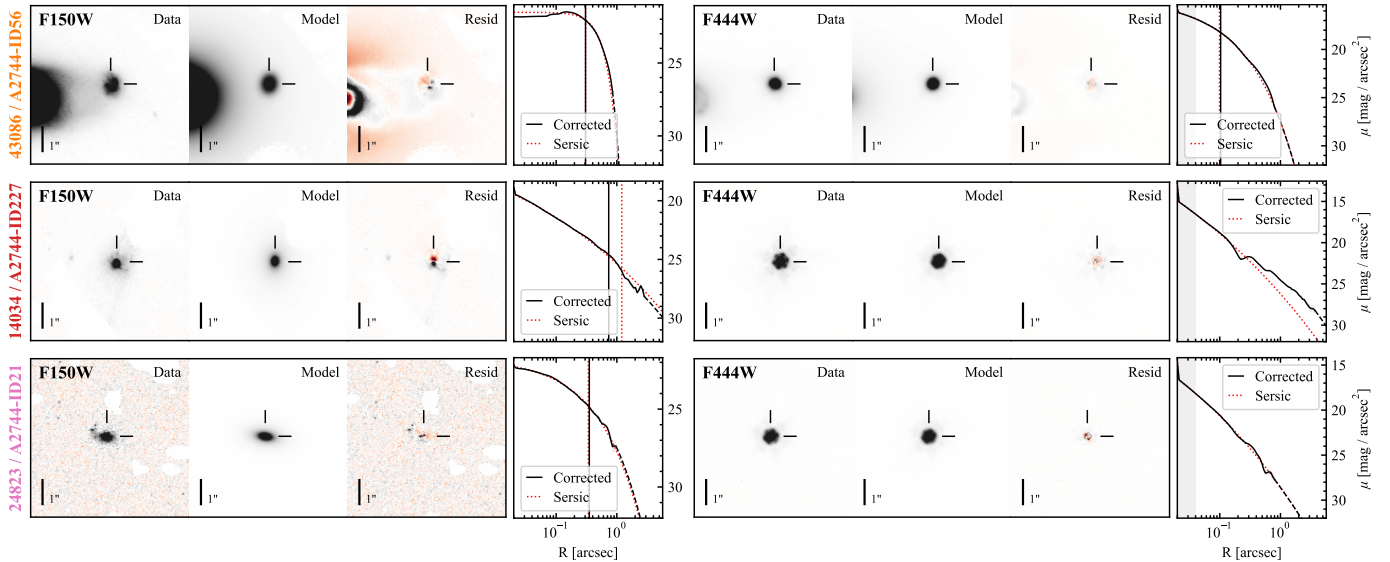


Figure 2. (cont.)

2002, 2010) on $8'' \times 8''$ cutouts (from the original resolution, non-PSF matched images) in all filters where the integrated galaxy flux has $\text{SNR} \geq 10$. First, we fit the parameters in F444W, using initial values based on the detection catalog and adopting parameter limits on the Sérsic index ($n_S = [0.2, 8]$), major axis effective radius ($R_{E,S} = [0.3, 300]$ pixels), and axis ratio ($b/a = [0.05, 1]$), while requiring the total magnitude to be within ± 3 mag and the center position to within ± 10 pixels of the initial values. We simultaneously fit any neighboring objects with $\min(\Delta\text{mag}_X) < 1.5$ (considered over all filters X) and with any part of their segmentation maps falling within $1.5''$ of the primary object, and mask all other detected objects using the detection segmentation maps. We then fit in all other filters in which the galaxy has $\text{SNR} \geq 10$, fixing the position and PA of all objects to the F444W values. For all filters, we flag the fit if GALFIT returns a flag > 0 or if one of the parameters reaches the enforced limit (with the exception that we do not flag fits where $n_S = 8$ or $b/a = 1$). Additionally, as some of our objects are nearly point sources in the reddest filters, we do not flag fits where only $R_{E,S}$ has numerical stability issues and $R_{E,S} < 1$ pixel.

We modify this procedure if $(b/a)_{\text{F444W}} > 0.75$, as the position angle (PA) may be poorly constrained. In this case, we fix the positions to the best-fit $(x_c, y_c)_{\text{F444W}}$ and perform an intermediate fit on the shortest-wavelength JWST filter with $\text{SNR} \geq 10$ to determine the galaxy's PA. After this SW filter fit, we refit F444W with the positions and PA of all objects fixed, and then fit all remaining filters as in the normal procedure. We show example short and long wavelength GALFIT model re-

sults for each object (F150W if fit and unflagged, otherwise F200W; and F444W) in the first three panels of the left and right columns in Fig. 2.

As single Sérsic component fits do not capture galaxy substructures (which are clearly present in many of the filters for galaxies in our sample), we also compute residual-corrected flux profiles and corrected effective radii R_E for all filters following Szomoru et al. (2010, 2012). We compute residual flux profiles from the GALFIT model residual images (masking all neighboring objects) using elliptical annular apertures with fixed PA and axis ratio based on each band's best-fit values. We then determine uncertainties using derived per-band empty aperture scaling relations (to capture correlated noise; as in Skelton et al. 2014). We show these residual-corrected and GALFIT Sérsic fit surface brightness profiles and respective effective radii ($R_E, R_{E,S}$) for example short and long wavelength bands (F150W or F200W and F444W) of each object in the fourth panel of each column in Fig. 4. We note that the parametric Sérsic $R_{E,S}$ are in fairly good agreement with the corrected R_E (median $R_E/R_{E,S} = 1.003$), suggesting that to at least first order the single-component fits capture the average light distributions fairly well, even in the presence of the observed substructures.

Because structural fitting is performed in the image plane, we must account for the lensing magnification on sizes. As our sample has only modest magnifications of $\mu \sim 2 - 4$, we correct for lensing with a factor of $1/\sqrt{\mu}$. Throughout this paper, all physical sizes have been corrected for both cosmology and this lensing factor. Angular sizes, as measured directly in the image plane, are uncorrected for lensing.

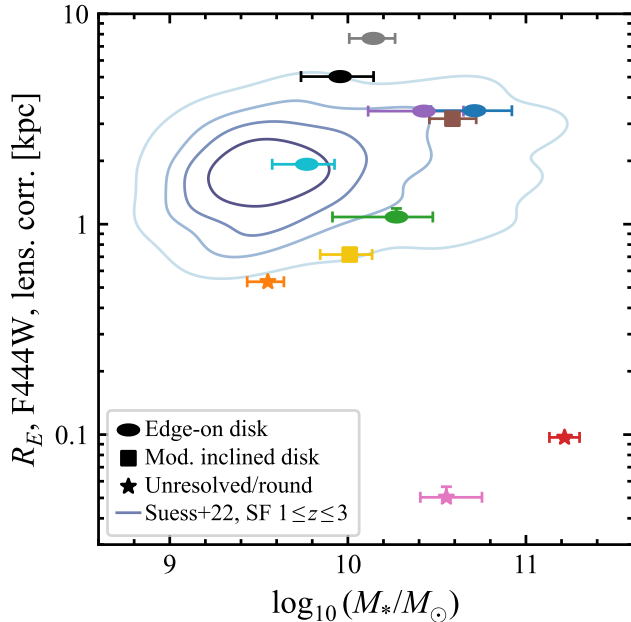


Figure 3. Stellar mass versus semi-major effective radius in F444W (corrected for lensing using a factor of $1/\sqrt{\mu}$). The symbols shapes denote the primary visual morphological categories of edge-on disks (ovals), moderately inclined disks (squares), and unresolved or small round sources (stars), with the same symbol color for each galaxy as in Figs. 1, 4. Compared to the sample of star-forming galaxies at $z \sim 1-3$ from Suess et al. (2022), roughly half of our sample lies within the scatter of mass versus size for “normal” star-forming galaxies. Three objects are notable outliers to larger (9018*) and smaller (14034, 24823) radii for their mass.

As an alternative to the parametric Sérsic index, we also derive the empirical concentration C as defined in Conelice (2003) for all filters. We calculate the concentration from the residual-corrected flux profiles, in order to mitigate the impact of PSF-broadening (compared to measuring C from the observed images).

4. RESULTS

Our multiwavelength $0.5 - 4.4\mu\text{m}$ imaging of these 11 ALMA-detected galaxies reveals a diversity of structures. Visual inspection (i.e., Figs. 1 & 2) reveals galaxies that appear to be large disks, both edge-on (9018*, 16790, 26131, 43148; see also Kokorev et al. 2023 for other analysis of 9018*/ID319, which Kokorev et al. report may be in the early phases of a merger with the compact companion to the West given its undisturbed disk morphology) and more face-on (24143*; see also Wu et al. 2023). The sample also includes other smaller galaxies that appear disk-like and edge-on (16840, 24852), a small galaxy that appears to be a moderately inclined disk with a misaligned dust lane

but may be irregular (21972), and small objects which are irregular at short wavelengths but appear extremely compact and round at long wavelengths, likely caused by an obscured AGN or nuclear starburst (43086, 14034, 24823).

Quantitatively, the sample also exhibits a wide range structural parameter values. In Fig. 3 we show $R_{E,F444W,kpc}$ versus inferred stellar masses for our sample. Our sample ranges from low ($\sim 10^{9.5}M_{\odot}$) to high ($\sim 10^{11}M_{\odot}$) stellar mass. We find some of the objects visually that are identified as large disks lie above the mass-size distribution of “normal” star-forming galaxies at $z \sim 1-3$ from Suess et al. (2022), while the remainder of edge-on and moderately-inclined disks fall within the scatter of the Suess et al. sample. Our unresolved/round galaxies include one object (with the lowest stellar mass) just barely below the population scatter, while the two most extremely small objects are more than $\times 10$ below the normal star-forming galaxies. In Fig. 4, we consider measured structural parameters (effective radius, axis ratio, and Sérsic index) as a function of wavelength. We find sizes R_E spanning 1 – 2 orders of magnitude at a given wavelength, axis ratios b/a spanning from $\sim 0.1 - 1$, and Sérsic indices ranging from $n_S \sim 0.2 - 1$ in HST/ACS F435W to $n_S \sim 0.5 - 8$ in JWST/NIRCam F444W. The three galaxies with the smallest R_E in F444W ($\lesssim 0.1''$) have sufficiently concentrated long-wavelength light distributions (as evidenced by their relatively high n_S) to exhibit visible diffraction spikes in the log-scale color images (Fig. 1).

We also observe common trends in the variation of the structural parameters with wavelength, as seen in Fig. 4 (showing both the measured structural parameters, *top*, and the trends normalized to the values in F444W, *bottom*). With increasing wavelength, we find R_E decreases and n_S generally increases, with each galaxy appearing more compact and concentrated at longer wavelengths. (We find a similar trend of increasing C with wavelength, in agreement with the n_S trend.) We also find the axis ratios do not drastically change with wavelength (i.e., varying only by $\sim 0.1 - 0.2$), with the exception of three objects that are extremely compact at long wavelengths (43086, 14034, 24823).

Changes in morphology with wavelength, or equivalently color gradients, reflect non-uniform dust distributions as well as relative age or metallicity changes. Color gradients thus provide a powerful probe of how galaxies assemble their stellar mass profiles (e.g., Suess et al. 2021, 2023). In these sub-mm detected galaxies, the color gradients are consistent with dust being the primary driver of observed color gradients and morphological changes with wavelength, as we will discuss later.

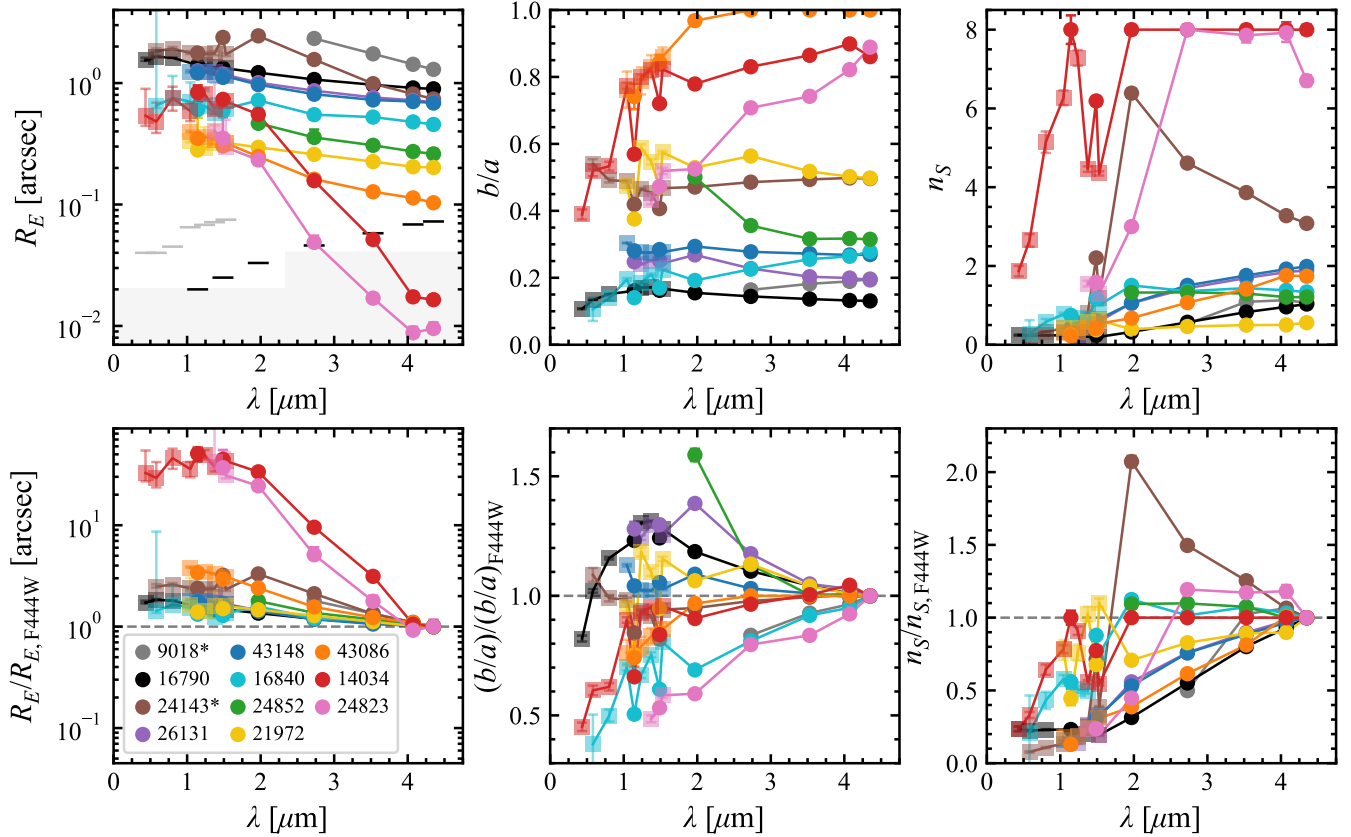


Figure 4. Measured structural parameters for all bands with good (unflagged) fits. The top row shows the corrected effective radius (R_E), axis ratio (b/a), and Sérsic index (n_S) versus filter wavelength (λ) (*left to right*, respectively). In the bottom row we plot the ratio of these values to the value measured from F444W. JWST and HST filters are denoted with solid circles and translucent squares, respectively, and in the upper left panel the horizontal black (grey) lines denote the HWHM of the JWST (HST) filter PSFs, and the filled light grey regions the pixel scale. The galaxies show a trend of decreasing R_E and increasing n_S towards longer wavelengths, consistent with a high central concentration of dust. Overall the axis ratios are broadly similar at all wavelengths, with the exception of three galaxies with the smallest $R_{E,LW}$ that are very round ($b/a \gtrsim 0.8$) at the longest wavelengths.

Thus to quantify the radial distribution of dust, we calculate a size ratio $\log_{10}(R_{E,LW}/R_{E,SW})$ between a long ($> 4\mu\text{m}$) and a short wavelength ($\sim 1.5 - 2.7\mu\text{m}$) band, probing the rest-frame NIR and optical, respectively, for this sample. We use F444W as the LW band, and preferentially use F150W (if the galaxy has sufficient SNR and an unflagged fit in that band), or otherwise F200W or F277W, as the SW band. These size ratios are shown as a function of F444W R_E in kpc (corrected for lensing using $1/\sqrt{\mu}$ as in Fig. 3), n_S , and C in Fig. 5. Our sample has size ratios that range from relatively mild values (~ -0.2), similar to those observed in $z \sim 1 - 3$ HST-selected star-forming galaxies by [Suess et al. \(2022\)](#), to extremely steep ratios (~ -1) for our extremely compact objects.

While we observe a correlation between $\log_{10}(R_{E,LW}/R_{E,SW})$ and $R_{E,F444W}$, where the smallest objects have the most extreme gradients, we find more

clear anti-correlations between $n_{S,F444W}$ and C_{F444W} and the size ratio. The [Suess et al. \(2022\)](#) sample also show slight tails of stronger gradients towards lower $R_{E,F444W}$ and higher $n_{S,F444W}$, though the observed trend for the sub-mm detected galaxies extends far beyond the region spanned by “typical” SFGs.

We also consider the size ratios versus stellar mass, $\log_{10}(M_*/M_\odot)$ (*fourth panel*). We find that \sim half of our sample roughly overlaps with the anti-correlation trend found by [Suess et al. \(2022\)](#), but the remainder of our objects have lower size ratios at a fixed stellar mass. This suggests that stellar mass alone does not set galaxies’ size ratios and that measures of long wavelength central concentration (i.e., C_{F444W} or $n_{S,F444W}$) correlate more strongly with size ratio (in contrast to [Gómez-Guijarro et al. 2023](#), who find dust concentration correlates most strongly with mass).

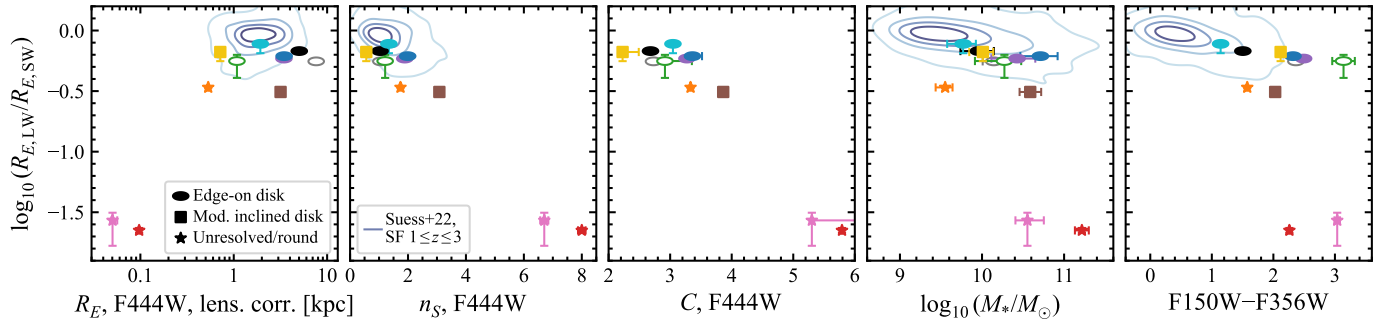


Figure 5. Ratio of long (F444W) to short wavelength (F150W if sufficient SNR and unflagged, solid symbols; otherwise F200W or F277W, open symbols) sizes, $\log_{10}(R_{E,LW}/R_{E,SW})$, as a function of structural and integrated color parameters. The symbols shapes are the same as in Fig. 3, with the same symbol color for each galaxy as in Figs. 1, 4. We plot these ratios versus R_E (lensing corrected), n_S , and the concentration C (as measured from the corrected flux profiles; see Sec. 3) from F444W (*first*, *second*, and *third* panels, respectively). Additionally, we plot against the inferred stellar mass (*fourth* panel), and against the observed integrated F150W–F356W color (*fifth* panel), which approximates the rest-frame V–J color given the sample redshift ($z \sim 2$). As a comparison, we also show the measured radii ratios $\log_{10}(R_{E,LW}/R_{E,SW})$ versus $R_{E,F444W}$, $n_{S,F444W}$, $\log_{10}(M_*/M_\odot)$, and V–J from Suess et al. (2022, colored contours). These comparisons demonstrate that our sample has size ratios (reflecting the color gradients and thus inferred dust attenuation gradients) extending from the range of “typical” $z \sim 1 - 3$ galaxies down to much more extreme values.

Finally, we examine the size ratios as a function of the integrated observed F150W–F356W color, which approximates the rest-frame V–J color for our sample redshift ($z \sim 2$; Fig. 5, *fifth* panel). Again, this is consistent with the anti-correlation of $\log_{10}(R_{E,LW}/R_{E,SW})$ with rest-frame V–J found by Suess et al. (2022). Our sample extends that trend to much more extreme red objects. In Fig. 5 we show that \sim half of our sample continues the $\log_{10}(R_{E,LW}/R_{E,SW}) - V-J$ trend shown by the Suess et al. contours; however, our sample also includes several objects that have significantly lower (i.e., 14034, 24823) size ratios than expected given their color (as also seen with stellar mass). As discussed earlier in this section, these objects have point-like LW morphologies which indicate that a central AGN or nuclear starburst may be driving these extremely low size ratios.

Rest-frame UVJ colors have been proposed to help distinguish between color gradients that are driven by dust versus age (e.g., Miller et al. 2022, 2023), though Leja et al. 2019 caution that interpretation of spatially-resolved UVJ colors with respect to dust gradients requires further testing. This analysis relies on the fact that more dust tends to produce redder U–V colors *and* redder V–J colors, whereas older ages tend to produce redder U–V colors but bluer V–J colors. To test our rest-frame color gradients, we use EAZY-Py (Brammer et al. 2008; using `tweak_fspz_QSF_12_v3` templates) to interpolate, or for 4 objects, slightly extrapolate, the residual-corrected deconvolved profiles shown in Fig. 2 to construct rest-frame UVJ color profiles. We find that all galaxies in our sample have both redder U–V and V–J colors in the centers than the outskirts, con-

sistent with increasing dust attenuation towards their centers. At face value this is consistent with high central dust concentrations, not older central stellar ages, particularly as we observe bright central NIR light ($\sim 15 - 20$ mag/arcsec²) and detect sub-mm emission. Future high-resolution sub-mm observations (e.g., with a forthcoming ALMA Cycle 10 program; PI: V. Kokorev) and spatially-resolved spectroscopy are needed to confirm the physical interpretation of observed color gradients.

5. DISCUSSION & CONCLUSIONS

This sample demonstrates that the population of sub-mm detected galaxies is not homogeneous in structure. Among our 11 objects, we observe disk-like structures over a range of inclinations and sizes, as well as smaller, more irregular objects that also host extremely compact central components at the longest wavelengths. In the rest-frame NIR (see Fig. 2), these structures are consistent with stellar disks (with a range of central concentrations; 8/11), small spheroidal or face-on stellar disks (1/11), and NIR continuum dominated by heavily obscured AGN or nuclear star clusters (2/11).

Even with this morphological diversity, we find evidence that within individual galaxies the dust and NIR continuum light distributions are similar. Specifically, we find the size ratios — and thus color gradients — correlate with size and concentration in F444W. As we find evidence that the color gradients are primarily driven by dust (Sec. 4), this correlation suggests that the objects with the smallest and most concentrated NIR continuum light (i.e., from obscured AGN or nuclear star-

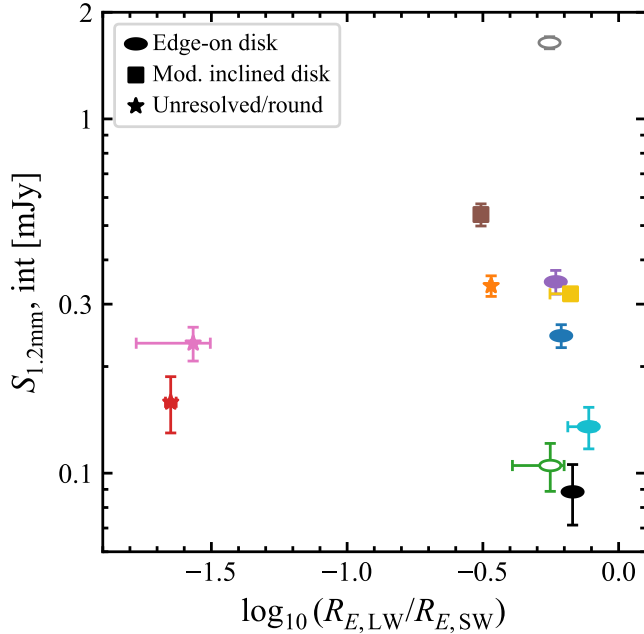


Figure 6. Comparison of the intrinsic, lensing-corrected ALMA 1.2mm flux density to the ratio of sizes $\log_{10}(R_{E,LW}/R_{E,SW})$ (using the same symbol definitions as in Fig. 5). We find the galaxies with the lowest size ratios (and smallest LW sizes) have some of the lowest flux densities, suggesting that compact dust geometry is responsible for these extreme size ratios. The objects with more mild size ratios (with a variety of sizes and axis ratios) exhibit a range of flux densities, suggesting that both dust geometry and total quantity impact their size ratios. However, the lack of galaxies in the high flux density, low size ratio region (where both dust geometry and quantity might impact the size ratios) may simply be due to our limited sample size and low survey volume, given the rarity of sources with flux densities > 1 mJy.

bursts) also have very small and compact dust distributions, while objects with less concentrated NIR light also have less concentrated dust. We see further evidence for self-similarity between the NIR continuum and dust distributions from the trend of axis ratios with wavelength: for most objects there is little change in b/a with wavelength, suggesting similar dust geometry to the underlying stellar distribution. For the objects hosting AGN or nuclear star clusters, the axis ratio changes reflect the emergence of these heavily obscured bright central components, also suggesting distribution self-similarity in order to hide these central components.

Finally, we find evidence that dust geometry, in addition to total dust quantity, is important in setting these galaxies’ multiwavelength structures. The objects with the lowest size ratios and most compact rest-frame NIR sizes (24823, 14034; with lensing corrected $R_E \lesssim 100$ pc

as in Fig. 5, left panel) have some of the lowest intrinsic 1.2 mm flux densities using updated fluxes from the recently released DUALZ catalog by Fujimoto et al. 2023b; Fig. 6). Low sub-mm fluxes can reflect low total dust quantity or lower incident radiation from, e.g., star formation or AGN activity. As the very centrally bright, physically compact NIR emission would suggest relatively high incident radiation, we thus infer the total dust quantity is low. Therefore, we argue that only through extremely compact dust distributions is it possible to reach sufficiently high dust column depths to drive these strong color and size gradients.

For the remainder of our sample, consisting of larger (lensing corrected $R_E \sim 0.5 - 8$ kpc), less concentrated objects with milder size ratios (and thus milder color gradients), our results provide evidence of contributions from both dust geometry and total dust quantity. Among the objects with low to moderate 1.2mm flux densities ($S_{1.2\text{mm}, \text{int}}$), there is a rough anti-correlation between the 1.2mm flux density and the size ratios, which could be explained by higher dust content generally leading to stronger color gradients (and thus lower size ratios). The 1.2mm-brightest galaxy (9018*; grey) does not follow this trend. However, its high total dust content and edge-on geometry render it optically thick even in the rest-frame NIR, as evidenced by the noticeable dust patches and lanes in the F444W imaging and the extremely high $A_V \sim 4$ across the galaxy reported by Kokorev et al. (2023). The extremely thick dust may conceal an even more compact stellar distribution than the F444W light, and thus the observed size ratio may be milder than the intrinsic ratio between the stellar mass distribution and rest-frame optical light. If the LW size is higher relative to the stellar size in this galaxy compared to the others, this could explain why its size ratio is higher than we might expect for its dust content. Taken together, the varied distribution of our sample’s 1.2mm flux densities versus size ratios supports our interpretation that dust geometry and total quantity can both play a role in setting a galaxies’ observed structure, again underscoring the heterogeneous nature of this population.

This analysis highlights the power of using high-resolution, deep NIR imaging from JWST to unravel the multi-wavelength, multi-component structures of extremely dusty galaxies, which were previously shrouded from view. More detailed observations and modeling to directly recover the stellar mass and dust distributions are necessary to better understand the structures of sub-mm detected galaxies. This type of spatially-resolved spectral energy distribution (SED) modeling would benefit dramatically from higher-resolution ALMA contin-

uum observations, which are forthcoming in an approved ALMA Cycle 10 program (2023.1.00626.S; PI V. Koko-rev). Resolved NIR spectroscopy (either from a slit or IFU) would also be critical to directly probe the reddening and thus detangle the dust, age, and metallicity color degeneracies. Future work with these observations will also determine how well dust and stellar geometries are captured through multiwavelength structural measurements similar to those presented in this work. Finally, JWST and ALMA will continue to map larger fields, including the recently completed ALMA Cycle 9 program DUALZ covering the full extended Abell 2744 cluster (Fujimoto et al. 2023b), yielding significantly larger samples that fully span the demographics of dust-obscured/sub-mm-detected galaxies across cosmic time. Larger samples would enable full explorations of sub populations and constrain their respective evolutionary pathways. Combined with parallel efforts to characterize structures of less extreme galaxy populations, these studies will continue bridging the gap between optical studies of relatively low dust galaxies and sub-mm studies of the most dusty galaxies.

This work is based in part on observations made with the NASA/ESA/CSA *James Webb Space Telescope*. These observations are associated with JWST-GO-2561, JWST-ERS-1324, and JWST-DD-2756. Support for program JWST-GO-2561 was provided by NASA through a grant from the Space Telescope Science Institute, which is operated by the Associations of Universities for Research in Astronomy, Incorporated, under NASA contract NAS5-26555. This research is also based on observations made with the NASA/ESA *Hubble Space Telescope* obtained from the

Space Telescope Science Institute, which is operated by the Association of Universities for Research in Astronomy, Inc., under NASA contract NAS 5–26555. These observations are associated with programs HST-GO-11689, HST-GO-13386, HST-GO/DD-13495, HST-GO-13389, HST-GO-15117, and HST-GO/DD-17231. All of the data presented in this paper were obtained from the Mikulski Archive for Space Telescopes (MAST) at the Space Telescope Science Institute. The specific observations used to produce these mosaics can be accessed via [10.17909/zn4s-0243](https://doi.org/10.17909/zn4s-0243). This paper makes use of the ALMA data: ADS/JAO. ALMA #2018.1.00035.L, #2019.1.00237.S, #2021.1.01246.S, and #2021.1.00407.S. ALMA is a partnership of the ESO (representing its member states), NSF (USA) and NINS (Japan), together with NRC (Canada), MOST and ASIAA (Taiwan), and KASI (Republic of Korea), in cooperation with the Republic of Chile. The Joint ALMA Observatory is operated by the ESO, AUI/NRAO, and NAOJ. VK acknowledges funding from the Dutch Research Council (NWO) through the award of the Vici Grant VI.C.212.036. PD acknowledges support from the Dutch Research Council (NWO) through the award of the VIDI Grant 016.VIDI.189.162 (“ODIN”) and the European Commission’s and University of Groningen’s CO-FUND Rosalind Franklin program.

Facilities: JWST (NIRCam), HST (ACS and WFC3), ALMA

Software: astropy (Astropy Collaboration et al. 2013, 2018, 2022), EAZY-Py (Brammer et al. 2008), GALFIT (Peng et al. 2002, 2010), matplotlib (Hunter 2007), numpy (Harris et al. 2020), scipy (Virtanen et al. 2020), seaborn (Waskom 2021), photutils (Bradley 2023), Prospector (Johnson et al. 2021)

REFERENCES

- Aravena, M., Decarli, R., Walter, F., et al. 2016, ApJ, 833, 68
- Astropy Collaboration, Robitaille, T. P., Tollerud, E. J., et al. 2013, A&A, 558, A33
- Astropy Collaboration, Price-Whelan, A. M., Sipőcz, B. M., et al. 2018, AJ, 156, 123
- Astropy Collaboration, Price-Whelan, A. M., Lim, P. L., et al. 2022, ApJ, 935, 167
- Barbary, K. 2018, SEP: Source Extraction and Photometry, Astrophysics Source Code Library, record ascl:1811.004, , , ascl:1811.004
- Bezanson, R., Labbe, I., Whitaker, K. E., et al. 2022, arXiv e-prints, arXiv:2212.04026
- Boogaard, L. A., Gillman, S., Melinder, J., et al. 2023, arXiv e-prints, arXiv:2308.16895
- Bradley, L. 2023, astropy/photutils: 1.8.0, Zenodo, v1.8.0, Zenodo, doi:10.5281/zenodo.7946442
- Brammer, G. 2019, Grizli: Grism redshift and line analysis software, Astrophysics Source Code Library, record ascl:1905.001, , , ascl:1905.001
- Brammer, G. B., van Dokkum, P. G., & Coppi, P. 2008, ApJ, 686, 1503

Table 1. Sample properties and structural parameters

ID	ID _{ALCS}	RA	Dec	z_{best}	Type	Ref.	μ	$\log_{10} M_*$	$R_{E,F444W}$	$n_{S,F444W}$	C_{F444W}	$\log_{10} \left(\frac{R_{E,LW}}{R_{E,SW}} \right)$
(1)	(2)	(3)	(4)	(5)	(6)	(7)	(8)	(9)	(10)	(11)	(12)	(12)
9018*	ID319	3.575986	-30.413174	2.580	1	3,9	1.85	$10.1^{+0.1}_{-0.1}$	$1.297^{+0.005}_{-0.003}$	1.06 ± 0.01	$2.729^{+0.222}_{-0.006}$	$-0.254^{+0.002}_{-0.001}, a$
16790	ID178	3.600396	-30.396138	0.940	2	1,5	1.98	$10.0^{+0.2}_{-0.2}$	$0.897^{+0.002}_{-0.001}$	1.03 ± 0.00	$2.681^{+0.001}_{-0.001}$	$-0.170^{+0.001}_{-0.001}$
24143*	ID33	3.584924	-30.381780	3.060	1	1,2,9	3.19	$10.6^{+0.1}_{-0.1}$	$0.740^{+0.013}_{-0.012}$	3.08 ± 0.01	$3.862^{+0.058}_{-0.007}$	$-0.507^{+0.010}_{-0.009}$
26131	ID07	3.579685	-30.378407	2.410	1	1,2,9	2.70	$10.4^{+0.2}_{-0.3}$	$0.697^{+0.010}_{-0.007}$	1.89 ± 0.01	$3.273^{+0.002}_{-0.002}$	$-0.231^{+0.008}_{-0.018}$
43148	ID47	3.571959	-30.382986	1.670	1	7,8	2.80	$10.7^{+0.2}_{-0.2}$	$0.685^{+0.004}_{-0.004}$	1.99 ± 0.01	$3.362^{+0.156}_{-0.001}$	$-0.211^{+0.004}_{-0.007}$
16840	ID176	3.572349	-30.395966	$3.65^{+0.09}_{-0.14}$	3	6	2.92	$9.8^{+0.2}_{-0.2}$	$0.457^{+0.020}_{-0.004}$	1.34 ± 0.01	$3.045^{+0.010}_{-0.008}$	$-0.110^{+0.024}_{-0.077}$
24852	ID17	3.581273	-30.380227	3.470	1	7,8	3.14	$10.3^{+0.2}_{-0.4}$	$0.261^{+0.026}_{-0.002}$	1.21 ± 0.00	$2.915^{+0.437}_{-0.007}$	$-0.252^{+0.051}_{-0.139}, a$
21972	ID81	3.582499	-30.385459	3.055	1	7,8	4.65	$10.0^{+0.1}_{-0.2}$	$0.202^{+0.006}_{-0.001}$	0.56 ± 0.00	$2.227^{+0.263}_{-0.001}$	$-0.177^{+0.013}_{-0.076}$
43086	ID56	3.573258	-30.383501	1.500	1	1,2,9	2.70	$9.6^{+0.1}_{-0.1}$	$0.103^{+0.001}_{-0.000}$	1.74 ± 0.03	$3.331^{+0.001}_{-0.001}$	$-0.470^{+0.003}_{-0.006}$
14034	ID227	3.568930	-30.402792	2.580	2	1,5	1.85	$11.2^{+0.1}_{-0.1}$	$0.016^{+0.000}_{-0.000}$	8.00 ± 0.13	$5.792^{+0.000}_{-0.000}$	$-1.650^{+0.020}_{-0.019}$
24823	ID21	3.592096	-30.380472	2.640	1	1,2,9	2.28	$10.6^{+0.2}_{-0.1}$	$0.010^{+0.001}_{-0.000}$	6.70 ± 0.14	$5.302^{+1.656}_{-0.000}$	$-1.567^{+0.063}_{-0.210}$

NOTE— (1) UNCOVER ID (DR2; Weaver et al. 2023). (2) ALCS ID (Fujimoto et al. 2023a), omitting the prefix ‘A2744’. (3) UNCOVER catalog coordinate (J2000). (4) Best available redshift. (5) Redshift type: 1: spectroscopic, 2: HST grism, 3: photometric. (6) References: 1: Fujimoto et al. (2023a), 2: Muñoz Arancibia et al. (2023), 3: Kokorev et al. (2023), 4: Laporte et al. (2017), 5: Wang et al. (2015), 6: Wang et al. (2023, UNCOVER, DR2 SPS catalog), 7: Fujimoto et al. (2023b, DUALZ), 8: S. Price et al., in prep (UNCOVER), 9: F. Bauer et al., in prep (ALCS). (7) Magnification (using the updated v1.1 model of Furtak et al. 2023). (8) Stellar mass from Prospector as in Wang et al. (2023), with fixed redshift when z_{spec} or z_{griz} is available and using alternative deblended photometry for noted objects (see Sec 2). (9) Residual-corrected major axis effective radius measured in F444W, uncorrected for lensing, in arcsec. (10) GALFIT Sérsic index in F444W. (11) Concentration parameter measured from the F444W residual corrected flux profiles. (12) Ratio of long to short wavelength residual-corrected effective radii. By default, F444W and F150W are used for the LW and SW radii, respectively. If F150W has insufficient SNR or a flagged fit, F200W or next F277W is used instead (noted with *a*). *Annotation*: *: Alternative detection and segmentation used for morphological analysis and stellar population modeling (see Sec. 2).

Calistro Rivera, G., Hodge, J. A., Smail, I., et al. 2018, ApJ, 863, 56
Casey, C. M., Narayanan, D., & Cooray, A. 2014, PhR, 541, 45
Cheng, C., Yan, H., Huang, J.-S., et al. 2022, ApJL, 936, L19
Cheng, C., Huang, J.-S., Smail, I., et al. 2023, ApJL, 942, L19
Conselice, C. J. 2003, ApJS, 147, 1
Dudzevičiūtė, U., Smail, I., Swinbank, A. M., et al. 2020, MNRAS, 494, 3828
Dunlop, J. S., McLure, R. J., Biggs, A. D., et al. 2017, MNRAS, 466, 861
Fujimoto, S., Ouchi, M., Ono, Y., et al. 2016, ApJS, 222, 1
Fujimoto, S., Kohno, K., Ouchi, M., et al. 2023a, arXiv e-prints, arXiv:2303.01658
Fujimoto, S., Bezanson, R., Labbe, I., et al. 2023b, arXiv e-prints, arXiv:2309.07834
Furtak, L. J., Zitrin, A., Weaver, J. R., et al. 2023, MNRAS, 523, 4568
Gardner, J. P., Mather, J. C., Abbott, R., et al. 2023, PASP, 135, 068001

Gillman, S., Gullberg, B., Brammer, G., et al. 2023, A&A, 676, A26
Gómez-Guijarro, C., Elbaz, D., Xiao, M., et al. 2022, A&A, 658, A43
Gómez-Guijarro, C., Magnelli, B., Elbaz, D., et al. 2023, A&A, 677, A34
Gonzaga, S., Hack, W., Fruchter, A., & Mack, J. 2012, The DrizzlePac Handbook
González-López, J., Bauer, F. E., Romero-Cañizales, C., et al. 2017, A&A, 597, A41
González-López, J., Novak, M., Decarli, R., et al. 2020, ApJ, 897, 91
Harris, C. R., Millman, K. J., van der Walt, S. J., et al. 2020, Nature, 585, 357
Hodge, J. A., & da Cunha, E. 2020, Royal Society Open Science, 7, 200556
Hodge, J. A., Swinbank, A. M., Simpson, J. M., et al. 2016, ApJ, 833, 103
Hodge, J. A., Smail, I., Walter, F., et al. 2019, ApJ, 876, 130
Hunter, J. D. 2007, Computing in Science and Engineering, 9, 90

- Johnson, B. D., Leja, J., Conroy, C., & Speagle, J. S. 2021, *ApJS*, 254, 22
- Kokorev, V., Brammer, G., Fujimoto, S., et al. 2022, *ApJS*, 263, 38
- Kokorev, V., Jin, S., Magdis, G. E., et al. 2023, *ApJL*, 945, L25
- Lang, P., Schinnerer, E., Smail, I., et al. 2019, *ApJ*, 879, 54
- Laporte, N., Bauer, F. E., Troncoso-Iribarren, P., et al. 2017, *A&A*, 604, A132
- Le Bail, A., Daddi, E., Elbaz, D., et al. 2023, arXiv e-prints, arXiv:2307.07599
- Leja, J., Tacchella, S., & Conroy, C. 2019, *ApJL*, 880, L9
- Liu, F. S., Jiang, D., Guo, Y., et al. 2016, *ApJL*, 822, L25
- Liu, F. S., Jiang, D., Faber, S. M., et al. 2017, *ApJL*, 844, L2
- Liu, Z., Morishita, T., & Kodama, T. 2023, *ApJ*, 955, 29
- Magnelli, B., Gómez-Guijarro, C., Elbaz, D., et al. 2023, arXiv e-prints, arXiv:2305.19331
- Miller, T. B., van Dokkum, P., & Mowla, L. 2023, *ApJ*, 945, 155
- Miller, T. B., Whitaker, K. E., Nelson, E. J., et al. 2022, *ApJL*, 941, L37
- Muñoz Arancibia, A. M., González-López, J., Ibar, E., et al. 2023, *A&A*, 675, A85
- Nelson, E. J., Suess, K. A., Bezanson, R., et al. 2023, *ApJL*, 948, L18
- Peng, C. Y., Ho, L. C., Impey, C. D., & Rix, H.-W. 2002, *AJ*, 124, 266
- . 2010, *AJ*, 139, 2097
- Popping, G., Pillepich, A., Calistro Rivera, G., et al. 2022, *MNRAS*, 510, 3321
- Puglisi, A., Daddi, E., Liu, D., et al. 2019, *ApJL*, 877, L23
- Rujopakarn, W., Dunlop, J. S., Rieke, G. H., et al. 2016, *ApJ*, 833, 12
- Rujopakarn, W., Williams, C. C., Daddi, E., et al. 2023, *ApJL*, 948, L8
- Skelton, R. E., Whitaker, K. E., Momcheva, I. G., et al. 2014, *ApJS*, 214, 24
- Smail, I., Dudzeviciute, U., Gurwell, M., et al. 2023, arXiv e-prints, arXiv:2306.16039
- Smith, D. J. B., Hayward, C. C., Jarvis, M. J., & Simpson, C. 2017, *MNRAS*, 471, 2453
- Suess, K. A., Kriek, M., Price, S. H., & Barro, G. 2019, *ApJ*, 877, 103
- . 2021, *ApJ*, 915, 87
- Suess, K. A., Bezanson, R., Nelson, E. J., et al. 2022, *ApJL*, 937, L33
- Suess, K. A., Williams, C. C., Robertson, B., et al. 2023, arXiv e-prints, arXiv:2307.14209
- Sun, F., Egami, E., Fujimoto, S., et al. 2022, *ApJ*, 932, 77
- Szomoru, D., Franx, M., & van Dokkum, P. G. 2012, *ApJ*, 749, 121
- Szomoru, D., Franx, M., van Dokkum, P. G., et al. 2010, *ApJL*, 714, L244
- Tadaki, K.-i., Belli, S., Burkert, A., et al. 2020, *ApJ*, 901, 74
- Virtanen, P., Gommers, R., Oliphant, T. E., et al. 2020, *Nature Methods*, 17, 261
- Wang, B., Leja, J., Labbé, I., et al. 2023, arXiv:2310.01276
- Wang, X., Hoag, A., Huang, K. H., et al. 2015, *ApJ*, 811, 29
- Waskom, M. 2021, *The Journal of Open Source Software*, 6, 3021
- Weaver, J. R., Cutler, S. E., Pan, R., et al. 2023, arXiv e-prints, arXiv:2301.02671
- Wu, Y., Cai, Z., Sun, F., et al. 2023, *ApJL*, 942, L1
- Wuyts, S., Förster Schreiber, N. M., Genzel, R., et al. 2012, *ApJ*, 753, 114
- Zhang, J., Wuyts, S., Cutler, S. E., et al. 2023, *MNRAS*, 524, 4128